Available online at www.sciencedirect.com
SCIENCE DIRECT®
International Journal of Thermal Sciences 45 (2006) 595–606
International Journal of Thermal Sciences
www.elsevier.com/locate/ijts

Heat and mass transfer during ice accretion on aircraft wings with an improved roughness model

Guy Fortin [a,*], Jean-Louis Laforte [b], Adrian Ilinca [a]

[a] *Groupe éolien, Université du Québec à Rimouski, 300 allée des Ursulines, Rimouski, PQ, Canada*
[b] *Laboratoire international des matériaux Anti-givre, Université du Québec à Chicoutimi, 555 Boulevard Université, Chicoutimi, PQ, Canada*

Received 1 September 2004; received in revised form 28 June 2005; accepted 3 July 2005

Available online 28 September 2005

Abstract

This paper presents the thermodynamic model used in the numerical simulation of ice accreted on an airfoil surface in wet and dry regimes developed at AMIL (Anti-Icing Materials International Laboratory), in a joint project with CIRA (Italian Aerospace Research Center). The thermodynamic model combines mass and heat balance equations to an analytical representation of water states over the airfoil to calculate the surface roughness and masses of remaining, runback, and shedding liquid water. The water state on the surface is represented in the form of beads, film or rivulets, each situation corresponding to a particular roughness height which has a major impact on the heat transfer coefficients necessary for the heat and mass balances. The model has been tested for severe icing conditions at six different temperatures corresponding to dry, mixed and wet accretion. Water mass, roughness and heat transfer convection coefficients over the airfoil surface are presented. The thermodynamic model combined with an air flow, water trajectory, and geometric model provides accurate results. It generates the complex ice shapes observed on the wing profile, and the numerical ice shapes profiles agree well with those obtained in wind tunnel experiments.

Keywords: Heat transfer; Mass transfer; Surface roughness; Convective heat; Water film; Ice accretion

1. Introduction

The simulation of ice accretion on airfoils is an iterative process that consists of the successive computation of airflow, water droplet trajectories, collection efficiency, and heat transfer balance to determine the shape of accreted ice. In this paper, the ice shapes are predicted using the 2D CIRAMIL code, which combines an aerodynamic algorithm developed by CIRA (Italian Aerospace Research Center) [1] and a thermodynamic model developed by AMIL (Anti-Icing Materials International Laboratory). The aerodynamic model used to determine the air flow around the airfoil is based on a potential flow approximation with a panel method and an integral boundary layer correction. Water droplet trajectories are determined from the inertial, gravitational and drag forces, which are used to find the collection efficiency, and then to determine the incoming quantity of water that hits each panel of the airfoil.

The thermodynamic model, based on the heat and mass transfer equations derived by Messinger [2], is used to determine the quantity of ice accreted on each panel of the airfoil. During ice accretion, roughness develops on ice-covered surfaces. The roughness controls the boundary layer development, which affects the convective heat transfer and the droplet collection efficiency, which in turn influence the ice shape. Even if the importance of this factor is well recognized, no study has been done to investigate the surface roughness associated with ice accretion. The lack of information in the matter has been circumvented in numerical simulations by means of empirical correlations calculating the height of surface roughness or convective heat transfer coefficients. These correlations are developed by comparing computed ice shapes with a set of experimental results, and selecting the surface roughness height or convective heat transfer coefficient that provides the best agreement with experimentation. These empirical correlations are currently used in most numerical models simulating airfoil ice

* Corresponding author.
E-mail address: gfortin@uqac.ca (G. Fortin).

1290-0729/$ – see front matter
doi:10.1016/j.ijthermalsci.2005.07.006

Nomenclature

A_p	panel surface	m^2
C_{cal}	calibration coefficient	
C_f	friction coefficient	
C_g	drag coefficient associated to the flow regime	
Cp_a	specific heat of air	J·kg^{-1}·K^{-1}
Cp_i	specific heat of ice	J·kg^{-1}·K^{-1}
Cp_w	specific heat of water	J·kg^{-1}·K^{-1}
d_d	median diameter volumetric droplet	m
D_{va}	water vapour diffusion coefficient in air	m^2·s^{-1}
f	solid fraction	
e_b	bead height	m
e_f	film height	m
$e_{f_{\min}}$	minimal film height	m
e_r	rivulet height	m
f	freezing fraction	
f_{bw}	bead liquid fraction	
g	gravitational acceleration	m·s^{-2}
F_g	gravitational force	N
F_w	wind force	N
F_σ	rigidity force	N
h_{cd}	conductive heat transfer coefficient	W·K^{-1}·m^{-2}
h_{cv}	convective heat transfer coefficient	W·K^{-1}·m^{-2}
h_{dif}	mass transfer coefficient by diffusion	m·s^{-1}
H	shape factor	
k_a	thermal conductivity of air	W·K^{-1}·m^{-2}
k_i	thermal conductivity of ice	W·K^{-1}·m^{-2}
LWC	liquid water content	kg·m^{-3}
Le	Lewis number	
L_f	latent heat of sublimation	J·kg^{-1}·K^{-1}
L_v	latent heat of vaporization	J·kg^{-1}·K^{-1}
m_{evap}	evaporation water mass	kg
m_i	ice mass	kg
m_{imp}	impinging water mass	kg
m_{rbin}	incoming runback water mass	kg
m_{rbout}	outgoing runback water mass	kg
m_{resw}	residual water mass	kg
m_{rmw}	remaining water mass	kg
m_{sh}	shedding mass	kg
m_{sub}	sublimation mass	kg
m_w	liquid water mass	kg
m_{wadm}	admissible liquid water mass	kg
P_a	air pressure	Pa
P_v	water vapour pressure	Pa
P_{vs}	saturated water vapour pressure	Pa
Pr	Prandtl number	
Q_{adh}	adiabatic heating	W
Q_{cd}	conduction heat	W
Q_{cv}	convective heat	W
Q_{evap}	evaporation heat	W
Q_f	solidification heat	W
Q_{kin}	kinetic heating	W
Q_{ss}	sensible heat	W
Q_{sub}	sublimation heat	W
r	recovery factor	
$Re_{\tau-\kappa}$	Reynolds number based on the friction speed	
Re_K	Reynolds number based on the roughness height	
R_g	ratio of gravitational and rigidity forces	
R_v	water vapour perfect gas constant	J·kg^{-1}·K^{-1}
R_W	ratio of wind and rigidity forces	
St	Stanton number	
St_κ	rough Stanton number	
t	time	s
T_a	air temperature	K
T_{al}	surface temperature at preceding time step	K
T_e	temperature at the edge of the boundary layer	K
T_f	freezing water temperature	K
T_{rec}	recovery temperature	K
T_{res}	residual temperature	K
T_s	surface temperature	K
T_∞	free stream temperature	K
U_∞	free stream velocity	m·s^{-1}
U_e	speed at the edge of the boundary layer	m·s^{-1}
U_κ	speed at the roughness level	m·s^{-1}
U_τ	friction speed	m·s^{-1}

Greek symbols

α_i	thermal diffusion coefficient of ice	m^2·s^{-1}
β	local collection efficiency	
δ_l	height of the boundary layer	m
δ_l^*	displacement thickness	m
Δb	panel width	m
Δs	panel length	m
Δt	time step	s
ϕ	relative humidity	
κ	roughness height	m
κ_s	equivalent sand grain roughness	m
ρ_a	air density	kg·m^{-3}
ρ_b	bead density	kg·m^{-3}
ρ_i	ice density	kg·m^{-3}
ρ_{ve}	density of the water vapour at the edge of the boundary layer	kg·m^{-3}
ρ_{vs}	density of the water vapour at the object's surface	kg·m^{-3}
ρ_w	water density	kg·m^{-3}
σ_w	water surface tension	N·m^{-1}
φ	panel inclination	°
θ_c	contact angle	°
θ_l	thickness of the quantity of movement in a laminar regime	m
θ_t	thickness of the quantity of movement in a turbulent regime	m
μ_a	dynamic viscosity of air	Pa·s
μ_w	dynamic viscosity of water	Pa·s
ν_a	kinematics viscosity of air	m^2·s^{-1}
τ_w	wall shear stress	Pa

accretion. This approach is helpful, but does not take into consideration the ice accretion physics and the actual condition of ice-covered airfoil surfaces. Indeed, one of the more used correlations in ice accretion is the Ruff correlation, which is presented in Shin et al. [3] and reported by Shin and Bond [4]. This correlation, based on the definition of equivalent sand grain roughness [5], is not truly representative of the size and the distribution of the local surface asperities, especially when they are covered by a water film [6]. Therefore, given the importance of roughness in the thermodynamic of the ice accretion process, especially in the wet growth regime, an analytical model based on physical parameters was developed, in which the roughness surface elements are represented as beads, as defined in Hansman and Turnock [7] and by Louchez et al. [8], or as a wave in the form of a film, as described by Al-Khalil et al. [9,10].

The iterative process involved in existing airfoil icing simulations helps to make the surface continuous and smooth, which further averages heights of roughness elements. To counter and minimize this effect, a new method based on the bisection of the angle between adjacent panels is introduced to add the mass of accreted ice as it grows.

The objective of this paper is to present a detailed analysis of the heat and mass transfer prevailing during ice accretion in wet and dry regimes using a new analytical model predicting roughness heights. Since it has been presented in detail in Ref. [11], only a brief explanation of the geometric accretion model is presented. The effects of these improvements on the simulation are shown by comparing the mass and shape of accreted ice with experimental and previously reported results on the same airfoil.

2. Mass balance

The heat and mass transfer model used in the model presented follows Messinger's [2] approach extensively employed in the prediction of ice accretion on airfoils. The different mechanisms of water mass transfer during ice accretion are described in Fig. 1.

The liquid water mass is the summation of the impinging liquid water mass, the incoming runback water mass, and the residual liquid water mass, reduced by the evaporated water mass:

$$m_w = m_{\text{imp}} + m_{\text{rbin}} + m_{\text{resw}} - m_{\text{evap}} \tag{1}$$

The first source of liquid water is the impingement of supercooled droplets present in the air. It is related to the local collection efficiency, the liquid water content and the free stream velocity:

$$m_{\text{imp}} = \beta \cdot LWC \cdot U_\infty \cdot A_p \tag{2}$$

The second source is the incoming runback water mass in wet regime, which is equal to the outgoing runback water mass of the preceding control volume. The outgoing runback water mass is equal to the difference between the liquid and the remaining water masses of the preceding control volume:

$$m_{\text{rbout}} = m_w - m_{\text{rmw}} \tag{3}$$

The third source is the remaining water mass in the control volume as determined in the preceding time step. This water remains over the ice surface because the aerodynamic and gravitational forces are not large enough to break the water surface tension. This remaining water mass is calculated using a mass balance based on water state (film, rivulets or beads) and maximum bead height.

For the film, the mass balance assumes that the film formed by the remaining water has a minimum film height as follows:

$$m_{\text{rmw}} = \rho_w \cdot A_p \cdot e_{f\,\min} \tag{4}$$

For the rivulet, the mass balance assumes that the remaining water mass is equal to that of the unfrozen rivulet, which is computed as the unfrozen film part:

$$m_{\text{rmw}} = \rho_w \cdot A_p \cdot e_f \cdot (1 - f) \tag{5}$$

The remaining water mass for the bead state is related to the admissible liquid water mass when the bead is fully grown. This admissible water mass corresponds to the quantity of water trapped in the volume between frozen beads. This mass is the same for all beads uniformly spread over the surface:

$$m_{\text{wadm}} = \rho_w \cdot (1 - f_{\text{bw}}) \cdot A_p \cdot e_b \tag{6}$$

The bead liquid fraction is determined when the bead is fully grown. It is the height ratio between the liquid part and the bead, to which is added the volume ratio between the bead and the frozen parts, and given by:

$$f_{\text{bw}} = \sqrt{\frac{\rho_b}{\rho_w} \cdot \frac{1-f}{3} \cdot \left[2 + \cos(\theta_c)\right]} + f \cdot \frac{\rho_b}{\rho_i} \cdot \frac{f_w}{3} \cdot \frac{2 + \cos(\theta_c)}{1 + \cos(\theta_c)} \tag{7}$$

Bead density is expressed in terms of the liquid and solid bead parts as follows:

$$\rho_b = \rho_i \cdot f + \rho_w \cdot (1 - f) \tag{8}$$

Ice density used in the calculation was determined by Laforte [12] for a rotating cylinder. This empirical equation is independent of the cylinder diameter, and is valid when the surface temperature is lower than the solidification temperature:

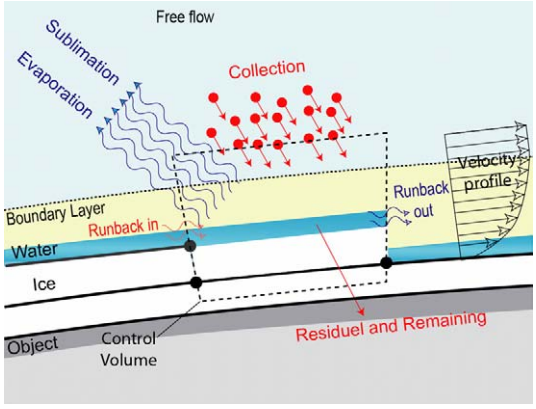

Fig. 1. Control volume mass balance for ice accretion.

$$\rho_i = 917\left(\frac{d_d \cdot U_\infty}{d_d \cdot U_\infty + 2.6\times 10^{-6}\ [\mathrm{m^2{\cdot}s^{-1}{\cdot}}K^{-1}]\cdot[T_f - T_s]}\right)^2 \tag{9}$$

As previously stated, the admissible liquid water mass is determined from the volume of the spaces between the frozen bead parts. When the liquid water does not completely fill the volume between beads, the remaining water mass is equal to the liquid water mass. When the liquid water fills the volume between the frozen bead parts completely, the remaining water mass is equal to the admissible liquid water mass:

$$m_{\mathrm{rmw}} = \begin{cases} m_{\mathrm{wadm}} & \text{if } m_w > m_{\mathrm{wadm}} \\ m_w & \text{if } m_w \leqslant m_{\mathrm{wadm}} \end{cases} \tag{10}$$

A small fraction of the liquid water mass evaporates in the air. The evaporation is a process which acts on the liquid water covering the object's surface. A water vapour concentration gradient is created in the boundary layer because of the water vapour concentration difference between the surface and the air at its boundary. Consequently, the evaporating water provides the necessary vapour to maintain the diffusion. The diffusion water mass is increased under the effect of the thermal gradient present in the boundary layer. The airflow temperature, being less than the surface temperature, the density of the water vapour contained in the air is constantly less than the density of the water vapour at the object's surface. This difference increases when the relative humidity is less than 100%. The mass lost by evaporation can be defined as a function of the mass transfer coefficient by diffusion, the water vapour density variation between the object's surface and the edge of the boundary layer, and the width and length of the control volume:

$$m_{\mathrm{evap}} = h_{\mathrm{dif}} \cdot (\rho_{\mathrm{vs}} - \rho_{\mathrm{ve}}) \cdot (\Delta b \cdot \Delta s) \cdot \Delta t \tag{11}$$

The water vapour density at the surface is calculated from the perfect gas law [13]. It depends on the water vapour pressure at the object's surface, the surface temperature and the water vapour constant. By definition, the water vapour at the surface is saturated:

$$\rho_{\mathrm{vs}} = \frac{P_{\mathrm{vs}}(T_s)}{R_v \cdot T_s} \tag{12}$$

The water vapour density at the boundary layer limit is also calculated from the perfect gas law. It depends on the water vapour pressure and the temperature at the edge of the boundary layer and the water vapour constant:

$$\rho_{\mathrm{ve}} = \frac{P_v(T_e)}{R_v \cdot T_e} \tag{13}$$

The relative humidity which is a meteorological term is defined as the ratio of the mass of the water vapour present in the air over the air's water vapour capacity [13], or, more commonly, air vapour pressure over the saturated vapour pressure:

$$\phi = \frac{P_v(T_e)}{P_{\mathrm{vs}}(T_e)} \tag{14}$$

The saturated vapour pressure, when expressed as a perfect gas [13], is a function of the solidification temperature of the water vapour gas constant and the latent heat of vaporization:

$$P_{\mathrm{vs}} = 610.8 \cdot e^{\frac{L_v}{R_v}\left(\frac{1}{T_f} - \frac{1}{T_a}\right)} \tag{15}$$

The diffusion mass transfer coefficient of vapour in air is determined from the analogy developed by Chilton–Colburn [14]. This coefficient is expressed as a function of the Lewis number, the air density and specific heat. The physical and thermal properties of air are evaluated at the boundary layer limit:

$$h_{\mathrm{dif}} = \frac{h_{\mathrm{cv}}}{\rho_a \cdot Cp_a \cdot Le^{2/3}} \tag{16}$$

The Lewis number is defined as the ratio of the Schmidt number over the Prandtl number. It is expressed as a function of the water vapour diffusion coefficient in air, air thermal conductivity, density and specific heat:

$$Le = \frac{k_a}{\rho_a \cdot Cp_a \cdot D_{\mathrm{va}}} \tag{17}$$

In dry regime, the impinging liquid water mass is the only term of the liquid water mass.

The liquid water freezes in fraction (wet regime) or in totality (dry regime) depending of heat balance. The ice mass is the solid fraction of the liquid water mass reduced by that lost by sublimation:

$$m_i = m_w \cdot f - m_{\mathrm{sub}} \tag{18}$$

When a fraction of the liquid water freezes, a part of the rest of the liquid water can remain on the ice surface whereas the other part run back over the surface to the next control volume.

The shedding water mass, which is the mass shed by the aerodynamic forces, should also be considered. It is assumed that liquid water behaves differently on the lower and upper surfaces. It was observed in numerical simulations that the upper surface is best characterized using a model with runback, while the lower surface is best characterized using a model without runback. Accordingly, a runback model is used on the upper and lower surfaces, but it is assumed that the runback water mass on the lower surface is shed by the aerodynamic force instead of moving to the next control volume. Therefore, the shedding water mass is zero on the upper surface while the runback water mass is zero on the lower surface:

$$m_{\mathrm{shw}} = \begin{cases} m_{\mathrm{rbout}} & \text{on the lower surface} \\ 0 & \text{on the upper surface} \end{cases} \tag{19}$$

3. Heat transfer during ice accretion

The energy conservation is applied on a control volume as shown at Fig. 2. The heat balance on each panel is the sum of the following energies: latent heat of solidification, evaporation and sublimation, sensible, convection, conduction and radiation heats, as well as adiabatic and kinetic heating. Heat is added to the surface mainly from the latent heat of fusion released during freezing, less from adiabatic heating induced by the aerodynamic heating, and to an even smaller extent from the kinetic energy of the droplets impacting the surface. Heat is removed from the surface principally by convection and evaporation when the surface is wet, and by convection and sublimation when the surface is dry, and to a lesser degree by conduction in the ice and by radiation in atmosphere. A fraction of the heat is

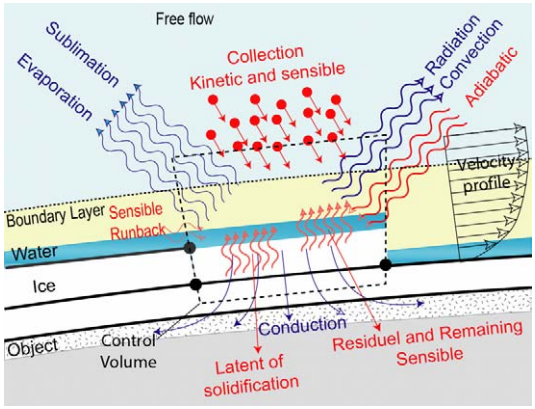

Fig. 2. Control volume energy balance for ice accretion.

used to bring the liquid water from the initial to the final temperature.

The steady-state assumption requires that the rate at which the energy is added to each control volume is equal to the rate at which it is removed:

$$Q_f + Q_{\text{adh}} + Q_{\text{kin}} = Q_{\text{ss}} + Q_{\text{sub/evap}} + Q_{\text{cd}} + Q_{\text{cv}} \tag{20}$$

When the water freezes, the transition from liquid to solid state gives off energy, in the control volume, known as the latent heat of solidification. The heat of solidification is the product of the mass of water that freezes on the panel during the time step and the latent heat of solidification:

$$Q_f = m_i \cdot L_f \tag{21}$$

The heat introduced by air friction on the object is from a viscous adiabatic heat which occurs inside the boundary layer. It is defined as the convective heat of the flow whose temperature goes from the free stream temperature to an average temperature known as the recovery temperature, and it is expressed as

$$Q_{\text{adh}} = h_{\text{cv}} \cdot (T_{\text{rec}} - T_\infty) \cdot (\Delta b \cdot \Delta s) \cdot \Delta t \tag{22}$$

The recovery temperature, T_{rec}, defined by Schlichting [15], is used for the sensible heat calculation. It consists of the average temperature of the boundary layer corrected as a function of the boundary layer air pressure for a non-conducting plate:

$$T_{\text{rec}} = T_\infty + r \cdot \frac{T_\infty}{T_e} \cdot \frac{U_e^2}{2 \cdot Cp_a} \tag{23}$$

The recovery factor, r, is a function of the Prandtl number and depends of the flow regime:

$$\text{For laminar flow } r = \sqrt{Pr} \quad \text{and}$$
$$\text{for turbulent flow } r = \sqrt[3]{Pr} \tag{24}$$

The sensible heat is provides by the temperature change of water and ice respectively. First it is calculated for the water that goes from initial temperature to the solidification temperature. Then, it considers the enthalpy variation of frozen and liquid water from the solidification temperature to the surface temperature. The initial temperature of the liquid water mass is that of the preceding time step and is referred as the residual temperature. The total sensible heat is given by

$$\begin{aligned} Q_{\text{ss}} &= m_w \cdot Cp_w \cdot (T_{\text{res}} - T_f) \\ &\quad + m_w \cdot f \cdot Cp_i \cdot (T_f - T_s) \\ &\quad + m_w \cdot (1 - f) \cdot Cp_w \cdot (T_f - T_s) \end{aligned} \tag{25}$$

The convection heat transfer is produced by the airflow over the wing's surface and is given by Newton's cooling law. The convective heat is expressed in terms of the convective heat transfer coefficient and the difference between the undisturbed flow temperature and the surface temperature:

$$Q_{\text{cv}} = h_{\text{cv}} \cdot (T_\infty - T_s) \cdot (\Delta b \cdot \Delta s) \cdot \Delta t \tag{26}$$

The calculation of the convective heat transfer coefficient is based on a modified Nusselt number. The former is expressed as a function of the Stanton number, the speed at the edge of the boundary layer, the air density, and its specific heat:

$$h_{\text{cv}} = \rho_a \cdot Cp_a \cdot U_e \cdot St \tag{27}$$

The Stanton number is defined using the Chilton–Colburn [14] analogy in laminar regime, and by the Spalding [16] analogy in turbulent regime, which takes into consideration the surface roughness.

The Chilton–Colburn analogy [14] defines the Stanton in laminar regime as a function of the friction coefficient and the Prandtl number:

$$St = 1/2 \cdot C_f \cdot Pr^{-2/3} \tag{28}$$

with Prandtl number defined as

$$Pr = \frac{\mu_a \cdot Cp_a}{k_a} \tag{29}$$

The friction coefficient for a flat plate can be written in laminar regime as a function of the kinematic viscosity, the speed at the edge of the boundary layer and the momentum thickness:

$$1/2 \cdot C_f = 0.225 \cdot \frac{v_a}{\theta_l \cdot U_e} \tag{30}$$

Spalding's analogy [16] defines the Stanton number for a rough flat plate in a turbulent regime as a function of the friction coefficient, the turbulent Prandtl number, and the rough Stanton number:

$$St = \frac{1/2 \cdot C_f}{0.9 + \sqrt{1/2 \cdot C_f} \cdot St_\kappa} \tag{31}$$

The rough Stanton number is defined as a function of Prandtl and Reynolds numbers:

$$St_\kappa = 1.92 \cdot Re_{\tau-\kappa}^{-0.45} \cdot Pr^{-0.8} \tag{32}$$

Here, Reynolds number is based on the roughness height, the friction speed and the kinematic viscosity of air:

$$Re_{\tau-\kappa} = \frac{U_\tau \cdot \kappa_s}{v_a} \tag{33}$$

The friction speed is proportional to the speed at the boundary layer limit and the friction coefficient in the turbulent regime:

$$U_\tau = U_e \cdot \sqrt{1/2 \cdot C_f} \tag{34}$$

The local friction coefficient [17] in the turbulent regime is a function of the momentum thickness and the roughness height:

$$1/2 \cdot C_f = \frac{0.1681}{[\ln(864 \cdot \frac{\theta_t}{\kappa_s} + 2.568)]^2} \tag{35}$$

The surface roughness accelerates the transition from a laminar regime to a transitional regime and affects the calculation of the local friction coefficient. Based on the work of Von Doenhoff [18], the transition from laminar to turbulent flow for a rough flat plate occurs when the Reynolds number, calculated from the equivalent roughness height (compared to that of sand paper), is equal to or greater than 600. The Reynolds number is calculated as a function of the speed at the roughness level, the height of the roughness, and the kinematic viscosity of air:

$$Re_\kappa = \frac{U_\kappa \cdot \kappa_s}{v_a} \tag{36}$$

The speed at the roughness level is equal to the speed at the boundary layer limit, when the roughness height is greater than the height of the boundary layer.

The boundary layer thickness for a flat plate in a laminar regime [15] is directly proportional to the displacement thickness

$$\delta_l = 3 \cdot \delta_l^* \tag{37}$$

and the shape factor [15], which is defined by the ratio of the displacement thickness and the thickness of the quantity of movement used to calculate the boundary layer position:

$$H = \frac{\delta_l^*}{\theta_l} \tag{38}$$

Otherwise, it is determined from the speed profile [15] in a laminar regime using the following approximate relation:

$$U_\kappa = \left(\frac{3}{2} \cdot \frac{\kappa_s}{\delta_l} - \frac{1}{2} \cdot \frac{\kappa_s^3}{\delta_l^3}\right) \cdot U_e \tag{39}$$

The evaporative heat is the product of the evaporated water mass and the latent heat of vaporization:

$$Q_{\text{evap}} = -m_{\text{evap}} \cdot L_v \tag{40}$$

The conductive heat loss is induced by the difference of temperature between the water film and the wing. It takes into consideration the heat transfer from the solid volume to the surface. Use of the de-icing system is not simulated, and the surface conduction heat is represented as a semi-infinite heated plate [19] assuming that:

- The axial heat transfer is minimal, especially in the impact area,
- the conductive heat transfer can be modeled while considering a semi-infinite surface since the penetration thickness is small when compared to the object's thickness,
- the limit condition, at the ice's surface, considers a stationary state with no surface movement, and the computing time, when the conduction effects are significant, is short when compared to the growth rate, making the hypothesis a valid approximation,
- the initial ice surface temperature is taken to be the same as the ambient temperature.

The heat loss by conduction can be expressed as a function of the conduction heat transfer coefficient, the difference between the surface temperatures at the preceding time step $(t - \Delta t)$, and the surface temperature at time t:

$$Q_{\text{cd}} = h_{\text{cd}} \cdot (T_{\text{al}} - T_s) \cdot (\Delta b \cdot \Delta s) \cdot \Delta t \tag{41}$$

The conduction heat transfer coefficient is derived from the thermal resistance normal to the surface in terms of time, ice thermal conductivity, and diffusion coefficients:

$$h_{\text{cd}} = \frac{k_i}{\sqrt{\pi \cdot \alpha_i \cdot t}} \tag{42}$$

The ice thermal diffusion coefficient is a function of its thermal conductivity, density, and specific heat:

$$\alpha_i = \frac{k_i}{\rho_i \cdot Cp_i} \tag{43}$$

3.1. Surface temperature

The surface temperature is calculated assuming a dry regime (solid fraction $f = 1$). If the resulting temperature is above the freezing point, a wet regime has to be considered using the computation of the solid fraction described in the following section. The surface temperature is the solution of a non-linear equation solved using Newton–Raphson iterative method:

$$T_s^{\text{new}} = T_s^{\text{old}} + \frac{f(T_s)}{\partial f(T_s)/\partial T_s} \tag{44}$$

Here, the energy equation (1) is written as $f(T_s) = 0$ in the form:

$$\begin{aligned} f(T_s) = {} & \big(L_f + Cp_w \cdot T_\infty + f \cdot (Cp_i - Cp_w) \cdot T_f \\ & - \big(f \cdot Cp_i + (1-f) \cdot Cp_w\big) \cdot T_s\big) \cdot \rho_w \cdot \frac{e_{\text{film}}}{\Delta t} \\ & + h_{\text{cv}} \cdot (T_\infty - T_s) + h_{\text{cd}} \cdot (T_\infty - T_s) \\ & + h_{\text{rad}} \cdot f_t \cdot (T_{\text{sky}} - T_s) + h_{\text{cv}} \cdot (T_{\text{rec}} - T_\infty) \\ & - h_{\text{dif}} \cdot \rho_{\text{vf}} \cdot L_{\text{vap}} \cdot \left(\frac{T_f}{T_s} \cdot e^{\frac{L_{\text{vap}}}{R_v}(\frac{1}{T_f} - \frac{1}{T_s})}\right. \\ & \left. - \phi \cdot \frac{T_f}{T_e} \cdot e^{\frac{L_{\text{vap}}}{R_v}(\frac{1}{T_f} - \frac{1}{T_a})}\right) \end{aligned} \tag{45}$$

3.2. Solid fraction

In a wet regime, when only a fraction f $(0 \leqslant f \leqslant 1)$ of the water solidifies, the surface temperature is equal to the water freezing temperature, and the solid fraction is determined by solving the energy conservation equation (1) written as:

$$\begin{aligned} f = {} & \frac{-1}{L_f \cdot \rho_w \cdot \frac{m_w}{\Delta t}} \cdot \left(h_{\text{cv}} \cdot (T_\infty - T_f) + h_{\text{cd}} \cdot (T_\infty - T_f)\right. \\ & + h_{\text{rad}} \cdot f_t \cdot (T_{\text{sky}} - T_f) \\ & + h_{\text{cv}} \cdot (T_{\text{rec}} - T_\infty) + Cp_w \cdot (T_\infty - T_f) \cdot \rho_w \cdot \frac{m_w}{\Delta t} \\ & \left. - h_{\text{dif}} \cdot \rho_{\text{vf}} \cdot L_{\text{vap}} \cdot \left(1 - \phi \cdot \frac{T_f}{T_e} \cdot e^{\frac{L_{\text{vap}}}{R_v}(\frac{1}{T_f} - \frac{1}{T_a})}\right)\right) \end{aligned} \tag{46}$$

4. Analytical model for roughness estimation

The height of the surface roughness is needed to determine the convection heat transfer coefficient. During ice accretion, the surface roughness height is unknown. Generally, an empirical correlation is used to estimate this height. In this paper, the roughness is determined using an analytical formulation for each one of the three possible liquid water states: film, bead or rivulet. A detailed description is presented in Fortin et al. [11].

4.1. Film

Film height is calculated by performing a mass balance over the control volume associated with each panel. Assuming that the flow is laminar [9], the film height is:

$$e_f = \sqrt{\frac{2}{\tau_w}} \cdot \sqrt{\frac{\mu_w \cdot m_w}{\rho_w \cdot \Delta b \cdot \Delta t}} \cdot C_{\text{cal}} \tag{47}$$

This equation was developed by Al-Khalil et al. [9] and used in thermal de-icing simulations. The calibration parameter, C_{cal}, is introduced to take into consideration the assumptions made to derive this equation which are: the film speed, calculated using Newton's viscosity law, and the wall shear stress is calculated using the friction coefficient in the laminar regime from Eq. (30) and in the turbulent regime from Eq. (35).

The surface water forms a film when its height is greater than the minimum film height, which corresponds to the maximum bead height multiplied by a shape factor. The maximum bead height is the height that the bead can reach before moving. The relation between the bead height and the film height is obtained from a mass balance, considering that the water film mass is equal to the summation of all the bead masses in the control volume. The minimum film height is given by

$$e_{f\,\min} = \sqrt{\frac{\theta_c - \sin(\theta_c) \cdot \cos(\theta_c)}{2 \cdot \sin(\theta_c)}} \cdot e_b \tag{48}$$

Roughness height is considered to be equal to the wave height [20] and given by

$$\kappa = \frac{3}{4} \cdot \frac{\tau_w}{\mu_w} \cdot \sqrt{\frac{e_f^3}{g}} \tag{49}$$

4.2. Beads

The water on the surface forms beads when the film height is less than the minimum film height and the control volume is in the impingement zone. In the bead model, it is assumed that the impinging droplets form beads on the surface upon impact.

In a wet regime (Fig. 3), the beads grow, being partially frozen and partially liquid. This growth ends when the beads reach a maximum height (the growth time for the case study is in the order of one second). At this moment, the liquid part runs, due to the aerodynamic force, a fraction of which remains trapped in the gaps between the frozen parts of the beads, while the rest flows and becomes runback water.

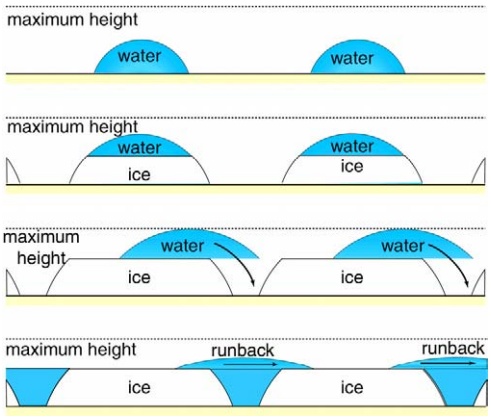

Fig. 3. Bead model in wet regime.

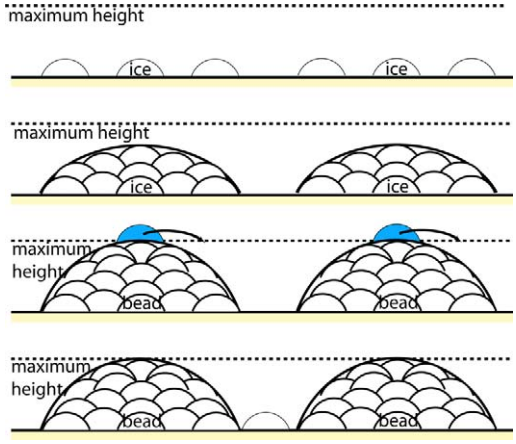

Fig. 4. Bead model in a dry regime.

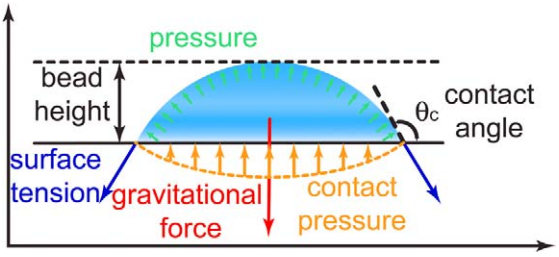

Fig. 5. Forces on a bead.

In a dry regime (Fig. 4), the droplets solidify entirely upon impact and the solidification time is in the order of a millisecond. New impinging droplets impact near other droplets to form growing beads. Growth ends when a maximum height is reached. At this time, the new droplets fall, under the aerodynamic force, between two solid beads; the solidification and the growth processes restart with a new bead.

Bead height is calculated from an analysis of the bead growth and the forces acting on it. Fig. 5 presents a two-dimensional view of a bead with a spherical shape characterized by height and contact angle. The forces acting on a bead are surface tension, gravity, and forces due to internal and contact pressures.

When the surface is inclined and/or wind is present (Fig. 6), disequilibrium is induced in the bead, which is deformed.

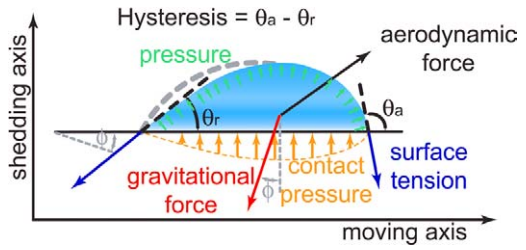

Fig. 6. Forces on a deformed bead.

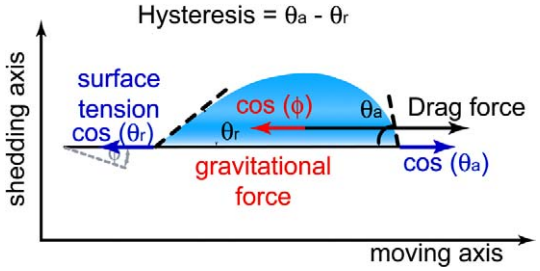

Fig. 7. Forces along the moving axis.

The bead becomes non-spherical and is characterized by an hysteresis, which is the difference between the maximum and minimum contact angles. The forces acting on the deformed bead are the same as in the previous case, to which drag and lift aerodynamic forces are added.

It is assumed that a bead moves only under the drag force, and there is not enough lift force to shed the bead. Bead height is a function only of the forces exerted along the moving axis. Assuming that the force due to internal pressure is negligible, the forces along the moving axis are the gravitational force component parallel to the surface; the rigidity force, which is the component of the surface tension along the moving axis in the direction opposite to the deformation; and the drag force, which is the aerodynamic force (Fig. 7).

Bead height is calculated from the following force balance along the moving axis:

$$\pm F_g \pm F_w - F_\sigma = 0 \tag{50}$$

When the maximum hysteresis is reached, the equilibrium between the aerodynamic, gravitational, and rigidity forces is broken and the bead begins to move. The maximum height that a bead can reach before moving is determined using the previous force equation for the maximum hysteresis condition. The contact angle and hysteresis on an ice surface have been measured as a function of temperature by Hansman and Turnock [7].

When the aerodynamic and gravitational forces are in the same direction, the roughness height is

$$e_b = \frac{-R_W \cdot C_G(e_b) + \sqrt{R_W^2 \cdot C_G^2(e_b) + 4 \cdot R_g \cdot \Delta\theta_c}}{2 \cdot R_g} \tag{51}$$

The gravitational flow ratio is the projection of the gravitational force parallel to the surface, divided by the rigidity force:

$$R_g = \frac{2}{3} \cdot g \cdot \frac{\rho_w}{\sigma_w} \cdot \left[\frac{2 + \cos(\theta_c)}{\sin^2(\theta_c)}\right] \cdot \left|\sin(\varphi)\right| \tag{52}$$

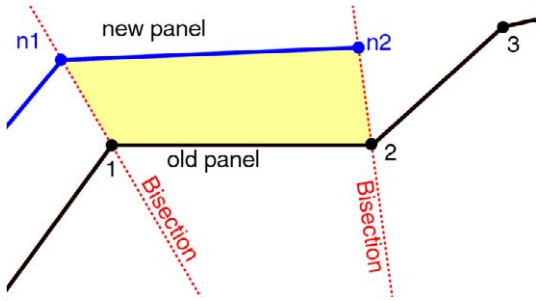

Fig. 8. Building of new panel.

The aerodynamic flow ratio is the projection of the aerodynamic force parallel to the surface divided by the rigidity force:

$$R_W = \frac{2}{\pi} \cdot \frac{\tau_w}{\sigma_w} \cdot \frac{\theta_c - \sin(\theta_c) \cdot \cos(\theta_c)}{\sin^2(\theta_c) \cdot [1 - \cos(\theta_c)]} \tag{53}$$

Roughness height is equal to the height that the bead reaches before moving:

$$\kappa = e_b \tag{54}$$

4.3. Rivulets

The water on the surface forms rivulets when the film height is less than the minimum film height, and the control volume is not exposed to impinging droplets. The surface is then wavy and rough. The rivulets are treated as small films of cylindrical form that flow parallel to the wind. The roughness height is equal to the rivulet height, which is assumed to be equal to the bead height before moving:

$$\kappa = e_r \tag{55}$$

5. Geometric accretion model

In general, ice shape is difficult to model when the growth direction is unknown. Therefore, the continuous bisection method was developed to eliminate the iterative process actually employed, which requires small panels and produces a smooth ice-covered surface. The use of the bisection method allows for ice to grow continuously in the direction normal to the surface of the object, which is the natural growth direction. To achieve this growth, the ice sections are limited by the bisection of angles with adjacent neighbouring panels. The continuous panel bisection method is illustrated in Fig. 8 and described in more details by Fortin et al. [11].

6. Results

6.1. Case studies

The 2D CIRAMIL code was evaluated by performing numerical simulations on a NACA0012 wing profile under the geometric, aerodynamic, and meteorological conditions shown in Table 1. The computation was performed at seven temperatures (−28.3, −19.4, −13.3, −10.0, −7.8, −6.1 and −4.4 °C) in both dry and wet regimes. The 2D CIRAMIL predicted ice

Table 1
Conditions for the numerical simulation

Accretion time	360 s
Angle of attack	4°
Chord	0.5334 m
Air speed	67.05 m·s^{-1}
Atmospheric pressure	101,300 Pa
Liquid water content	1 g·m^{-3}
Median volumetric diameter	20 mm

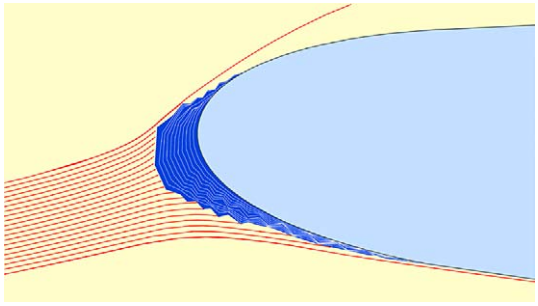

Fig. 9. Droplets trajectory.

shapes are compared to those obtained experimentally under the same conditions in the NASA Lewis Icing Research Tunnel (IRT) and those predicted using the 2D LEWICE/IBL code, presented in Shin and Bond [4]. They are also compared to the ice shapes predicted using the 2D CIRA code presented in reference [1]. Repeatability of the Shin and Bond [4] experimental ice shapes is for two runs, but no standard code error is given. The comparison between predicted and measured ice shapes can only be qualitative, as in most papers on the subject. In the IRT wind tunnel, the wing was vertical, meaning that gravitational acceleration was perpendicular to the wind. For the model, bead height is calculated for a flying configuration where the gravity acceleration component and wind are in the same direction. However, this equation can be used for the IRT wind tunnel where the gravitational force is small compared to the drag force. For this comparison, the predicted and measured ice shapes are those presented after six minutes of accretion. The liquid water mass and the roughness height distribution for the final time step are presented as a function of the curvilinear abscissa. The curvilinear abscissa follows the airfoil surface starting at the stagnation point. It has positive values for the upper surface and negative ones for the lower surface.

Fig. 9 shows the 4° attack angle of the wing and the supercooled water droplets trajectories which impact the iced surface at the temperature of −28.3 °C after 6 minutes of accretion.

6.2. Liquid water mass

Figs. 10 and 11 show the liquid water mass distribution in the control volume calculated for the final time step at −28.3 and −4.4 °C. In the dry regime at −28.3 °C (Fig. 10), the input liquid water mass originates from the impinging droplets only.

In the wet regime, at −4.4 °C (Fig. 11) on the upper surface, the input liquid water mass originates from the impinging droplets as well as the remaining and runback water masses. On

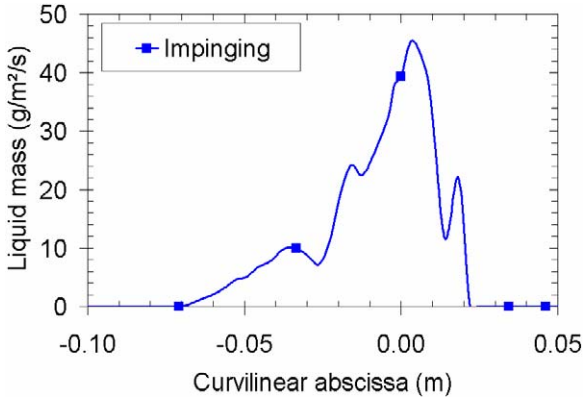

Fig. 10. Liquid water mass at −28.3 °C.

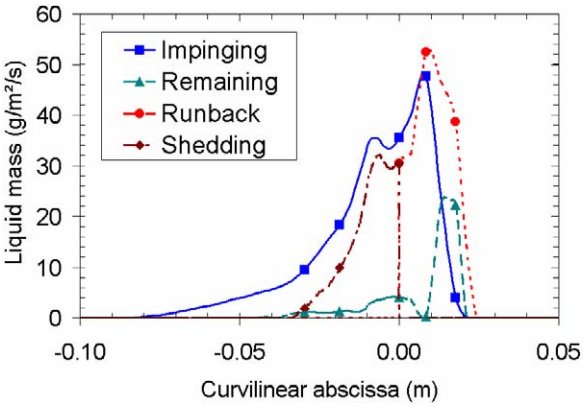

Fig. 11. Liquid water mass at −4.4 °C.

the lower surface, the input liquid water mass is composed of impinging droplets and remaining water, since all runback water is assumed to be shed by aerodynamic force. Gravity is not considered since the wing orientation with the wind tunnel is perpendicular to the gravity force.

6.3. Roughness height

Fig. 12 shows the roughness height distribution calculated at −4.4 and −28.3 °C for the final time step. In dry regime at −28.3 °C, supercooled water droplets freeze on impact and form beads on the surface. The roughness height is at a maximum at the stagnation point and decreases towards the ice end. In wet regime at −4.4 °C, the liquid water on the upper surface flows to the next control volume as a film, and the roughness is the wave height. For the lower surface, near the stagnation point, the liquid water, before shedding, is a film. For this flow state, the roughness height is at a minimum at the stagnation point. For the upper surface, this value increases sharply to reach a maximum, after which it decreases towards the ice end.

The roughness results are summarized in Table 2. In dry regime, the maximum roughness height is greater on the lower surface than on the upper surface, and it is independent of temperature.

In wet regime, the maximum roughness height is greater on the upper than on the lower surface. On the upper surface, this

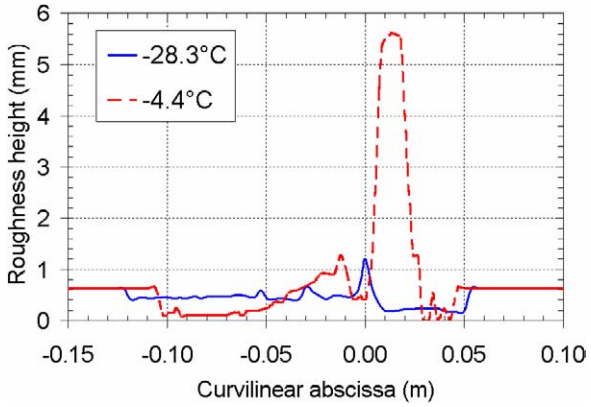

Fig. 12. Roughness distribution.

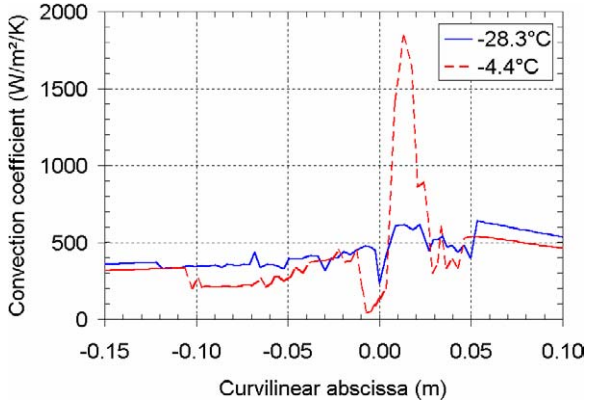

Fig. 13. Heat transfer convection coefficient.

Table 2
Roughness height at the final time step

Temperature	Regime	Upper		Lower	
		Max	Avg	Max	Avg
−28.3 °C	dry	–	0.23	–	0.48
−19.4 °C	dry	–	0.21	–	0.44
−13.3 °C	wet	3.34	0.09	1.20	0.40
−10.0 °C	wet	3.70	0.05	1.95	0.24
−7.8 °C	wet	5.62	0.03	1.41	0.19
−6.1 °C	wet	4.95	0.04	1.19	0.14
−4.4 °C	wet	4.65	0.02	1.27	0.13

height increases and reaches a maximum, after which it decreases. On the lower surface, this height decreases and reaches a minimum, after which it increases. On the upper surface, the average roughness height is independent of the temperature and is very small, while on the lower surface, it decreases with increasing temperature.

6.4. Heat transfer coefficient

Fig. 13 shows the heat transfer convection coefficient calculated for the final time step at −28.3 and −4.4 °C. In both cases, the heat transfer convection coefficient is at a minimum at the stagnation point. It increases to a maximum near the stagnation point to decrease toward the ice end. In dry regime, the coefficient is 230 $W{\cdot}m^{-2}{\cdot}K^{-1}$ at the stagnation point, and on the upper surface, increases to a maximum value of 615 $W{\cdot}m^{-2}{\cdot}K^{-1}$ from which it decreases gently to a value of 399 $W{\cdot}m^{-2}{\cdot}K^{-1}$. On the lower surface, it increases to a maximum value of 478 $W{\cdot}m^{-2}{\cdot}K^{-1}$ and decreases to a value of 333 $W{\cdot}m^{-2}{\cdot}K^{-1}$. In wet regime, the coefficient is 50 $W{\cdot}m^{-2}{\cdot}K^{-1}$ at the stagnation point, and on the upper surface, increase to a maximum value of 1842 $W{\cdot}m^{-2}{\cdot}K^{-1}$ and decreases rapidly afterward to a value of 300 $W{\cdot}m^{-2}{\cdot}K^{-1}$. On the lower surface, it increases to a maximum value of 449 $W{\cdot}m^{-2}{\cdot}K^{-1}$ and decreases to a value of 215 $W{\cdot}m^{-2}{\cdot}K^{-1}$.

6.5. Ice accretion shapes

Figs. 14–20 show the ice shapes predicted after six minutes of simulation using the 2D CIRAMIL, 2D LEWICE/IBL [21] and 2D CIRA [1] codes, which are compared to those measured experimentally by Shin and Bond [4]. For the −28.3 °C (Fig. 14) and −19.4 °C (Fig. 15) cases, ice shapes are typical of a dry regime where only rime ice forms. Predicted and measured ice shapes are essentially the same, except for the predicted volume, which is slightly greater than that measured. No significant difference can be observed between the 2D CIRAMIL, 2D LEWICE/IBL and 2D CIRA codes, except for the 2D LEWICE/IBL code, for which the ice volumes are slightly greater than those of the measured shapes. For the other cases (−13.3 °C, Fig. 16; −10.0 °C, Fig. 17; −7.8 °C, Fig. 18; −6.1 °C, Fig. 19 and −4.4 °C, Fig. 20), the predicted ice shapes are typical of a wet regime, where horns form on the upper surface with a small hollow at the stagnation point. Both predicted and measured ice shapes look similar, however predicted volumes are slightly greater than those measured. For temperatures lower than, or equal to, −7.8 °C, the 2D CIRAMIL predicted ice shapes are closer to those measured than for the 2D LEWICE/IBL and 2D CIRA codes.

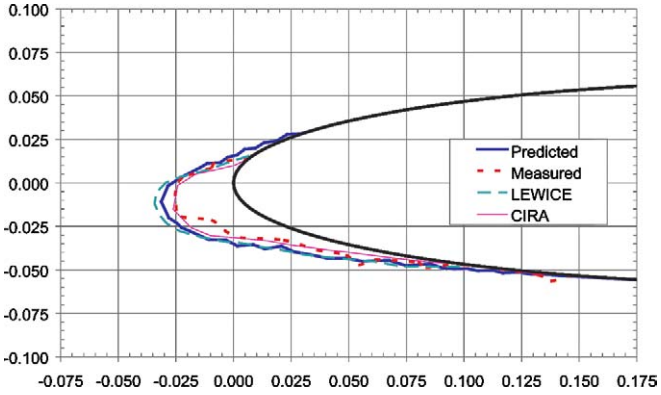

Fig. 14. Ice shape at −28.3 °C.

For temperatures above −7.8 °C, the 2D CIRAMIL code cannot produce the horn on the upper surface, as well as the 2D LEWICE/IBL and 2D CIRA codes. In most cases, the ice profiles are jagged along the wing in the region where the ice ends, because the ice mass shows a non-uniform growth.

In the three cases above −7.8 °C, the predicted and measured points where the ice ends are not located at the same

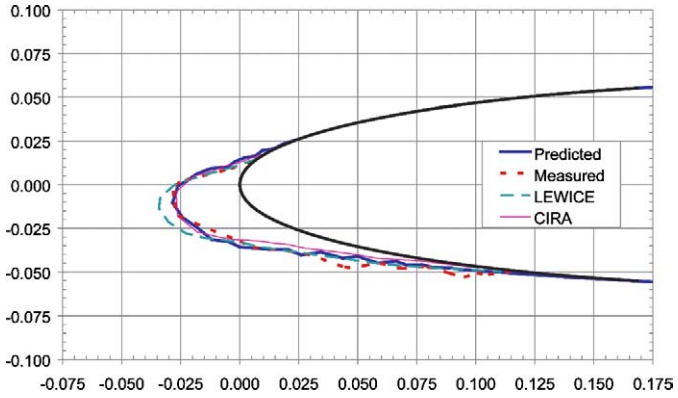

Fig. 15. Ice shape at −19.4 °C.

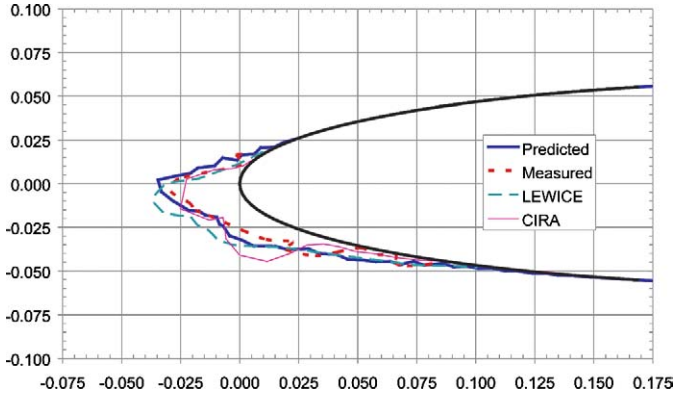

Fig. 16. Ice shape at −13.3 °C.

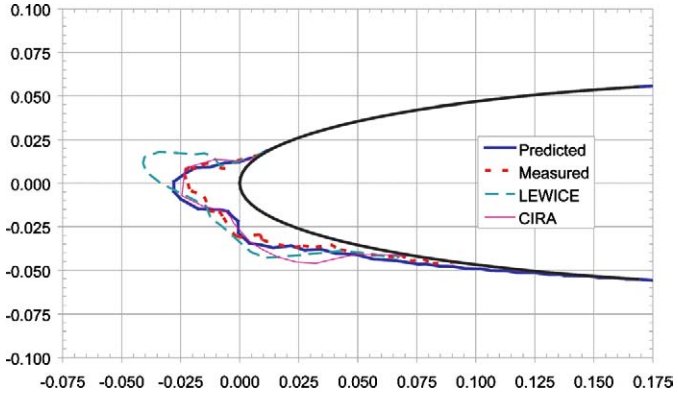

Fig. 17. Ice shape at −10.0 °C.

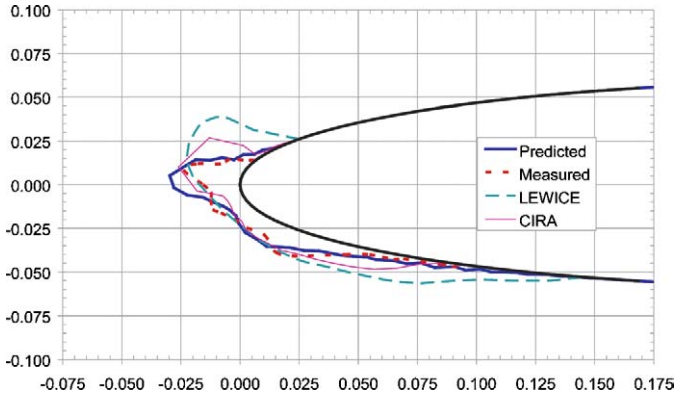

Fig. 18. Ice shape at −7.8 °C.

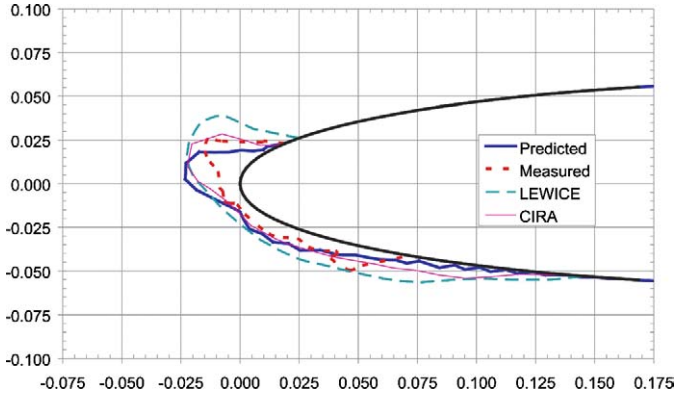

Fig. 19. Ice shape at −6.1 °C.

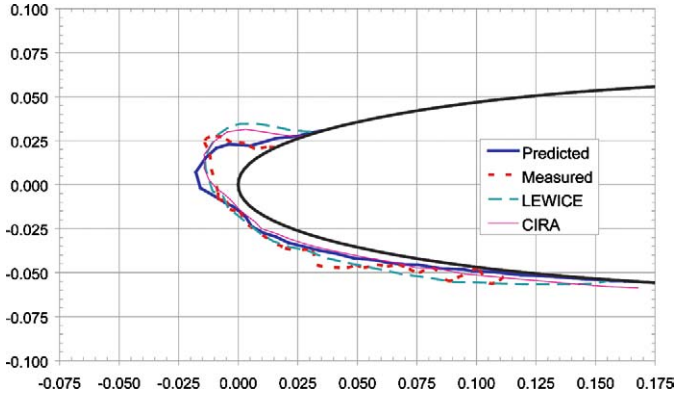

Fig. 20. Ice shape at −4.4 °C.

position. At −4.4 °C, the predicted and measured ice shapes are similar on the lower surface, but different on the upper surface because the horn is not formed in the same place. At −7.8 °C, the predicted and measured ice shapes are similar. This case was chosen to calibrate the roughness model because it corresponds to accretion grown in a half dry and half wet regime. The calibration was performed by adjusting parameter, C_{cal}, to a value of 15, where a better ice shape fit is obtained. This is probably due to the fact that the local roughness is too low, resulting in a too small local convective heat transfer coefficient.

7. Analysis

7.1. Thermodynamic model

The model can predict ice shapes on the leading edge of an airfoil are comparable to those obtained experimentally, and, in some cases, they fit better than those obtained with the available models. The predicted ice shapes are similar to those measured, with similarity increasing as temperature decreases. The maximum value of the convective heat transfer coefficient is found on the upper surface where the horn forms. As observed exper-

imentally, the length of the wet zone near the stagnation point increases with temperature.

7.2. Heat transfer coefficient

The model proposed to calculate the heat transfer coefficient combined to the roughness and mass model yields a good representation of ice shapes measured in a wind tunnel. The heat transfer coefficient distribution follows the roughness distribution with some difference due to the speed distribution. This difference can favour formation of horn and surface asperities where roughness and local convective heat transfer coefficients are higher.

7.3. Mass models

The free water flows as a film, beads, or rivulets on the upper surface, and is shed on the lower surface. A small quantity of water resides on the surface, depending on the intensity and direction of aerodynamic and gravitational forces. The runback water mass on the upper surface and the shedding water mass on the lower surface increase with temperature, as well as the remaining water mass. The ice accretion mass and volume decrease as temperature increases, while its density increases with temperature.

8. Conclusions

Based on the final ice shapes, the analytical model developed that includes local roughness height, remaining and shedding water masses, as well as the bisection method, can generate the complex ice shapes with horns observed experimentally with the same accuracy as, or better then, available models. However, in most cases, the predicted ice volume is slightly larger than the one measured. The predicted ice shapes obtained by the numerical simulation show that the runback water is dominant on the upper surface, while shedding water dominates on the lower surface. The ice shape is strongly dependent on the local roughness, which is directly related to the friction coefficient and, indirectly, to the convective heat transfer coefficient.

Acknowledgements

This work was financed mainly by AMIL. The financial support from NSERC through a postdoctoral fellowship and a research grant is kindly acknowledged. The authors would like to thank CIRA, who provided the airflow, droplet trajectory and collection efficiency codes. We also thank Patrick Louchez who started the project.

References

[1] G. Mingione, V. Brandi, Ice accretion prediction on multielements airfoils, J. Aircraft 35 (2) (1998).
[2] B.L. Messinger, Equilibrium temperature of an unheated icing surface as a function of airspeed, J. Aeronautic. Sci. 20 (1) (1953) 29–42.
[3] J. Shin, B. Berkowitz, H. Chen, T. Cebeci, Prediction of ice shapes and their effect on airfoil performance, American Institute of Aeronautics and Astronautics, Paper 91-0264, 1991.
[4] J. Shin, T. Bond, Experimental and computational ice shapes and resulting drag increase for a NACA 0012 airfoil, NASA Technical Manual 105743, January 1992.
[5] J. Nikuradse, Strö in Rauher Rohen, VDI-Forshungsheft 361, 1933, also Laws of Flow in Rough Pipes, NACA Technical Memorandum 1292, 1950.
[6] J. Shin, Characteristics of surface roughness associated with leading edge ice accretion, J. Airccraft 33 (2) (1996) 316–321, also AIAA Paper 94-0799, 1994.
[7] R.J. Hansman Jr, S.R. Turnock, Investigation of surface water behavior burring glaze ice accretion, J. Aircraft 26 (2) (1989) 140–147, also AIAA Paper 88-0015, January 1988.
[8] P. Louchez, G. Fortin, G. Mingione, V. Brandi, Beads and rivulets modelling in ice accretion on a wing, in: 36th AIAA Aerospace Sciences Meeting & Exhibit, January 12–15, Reno, Nevada, AIAA-98-0489, 1998.
[9] K.M. Al-Khalil, T.G. Keith, K.J. De Witt Jr, J.K. Nathman, D.A. Dietrich, Thermal analysis of engine inlet anti-icing systems, J. Propulsion Power 6 (1990) 628–634, also AIAA 89-0759 Paper, January 1989.
[10] K.M. Al-Khalil, T.G. Keith Jr, K.J. De Witt, Further development of an anti-icing runback model, in: 29th Aerospace Sciences Meeting & Exhibit, AIAA-91-0266, Reno, Nevada, January 1991, American Institute of Aeronautics and Astronautics, 1991, pp. 12.
[11] G. Fortin, A. Ilinca, J.-L. Laforte, V. Brandi, New roughness computation method and geometric accretion model for airfoil icing, J. Aircraft 41 (1) (2004) 119–127.
[12] J.-L. Laforte, M.A. Allaire, Évaluation du givromètre d'Hydro-Québec à différentes intensités de givrage sec et humide, in: Hydro-Québec, Études et Normalisation Équipement de Transport, Montréal, Québec, Canada, Rapport HQ-92-02, janvier 1992, pp. 2.1–2.5.
[13] M.D. Burghardt, Engineering Thermodynamics with Applications, third ed., Harper & Row, New York, 1986.
[14] F. Kreith, W.Z. Black, Basic Heat Transfer, Harper & Row, New York, 1980, pp. 218–219 and 486–489.
[15] H. Schlichting, Boundary-Layer Theory, McGraw-Hill, New York, 1979, pp. 337–339 and 713–715.
[16] F.M. White, Viscous Fluid Flow, Mechanical Engineering, second ed., McGraw-Hill, New York, 1991.
[17] T. Cebeci, P. Bradshaw, Physical and Computational Aspects of Convective Heat Transfer, New York, 1984.
[18] A.E. Von Doenhoff, E.A. Horton, A low-speed experimental investigation of the effect of a sandpaper type of roughness on boundary-layer transition, NACA Technical Manual 1349, 1958.
[19] R.B. Bird, W.E. Stewart, E.N. Lightfoot, Transport Phenomena, John Wiley & Sons, New York, 1960, pp. 352–354.
[20] P.M. Gerhart, R.J. Gross, J.I. Hochstein, Fundamentals of Fluid Mechanics, second ed., Addison-Wesley, Reading, MA, 1992, pp. 845–847.
[21] W.B. Wright, Users manual for the improved NASA Lewis ice accretion code LEWICE 1.6, National Aeronautical and Space Administration (NASA), Contractor Report, May 1995, pp. 95.